

pubs.acs.org/JACS Article

Pt Atomic Single-Layer Catalyst Embedded in Defect-Enriched Ceria for Efficient CO Oxidation

Shaohua Xie, [¶] Liping Liu, [¶] Yue Lu,* Chunying Wang, Sufeng Cao, Weijian Diao, Jiguang Deng, Wei Tan, Lu Ma, Steven N. Ehrlich, Yaobin Li, Yan Zhang, Kailong Ye, Hongliang Xin,* Maria Flytzani-Stephanopoulos, and Fudong Liu*



Cite This: https://doi.org/10.1021/jacs.2c08902



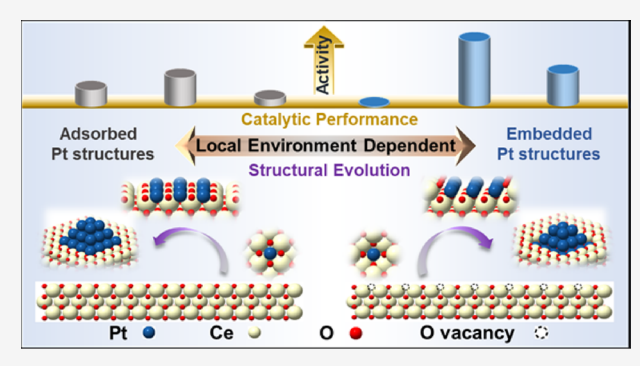
ACCESS

Metrics & More

Article Recommendations

Supporting Information

ABSTRACT: The local coordination structure of metal sites essentially determines the performance of supported metal catalysts. Using a surface defect enrichment strategy, we successfully fabricated Pt atomic single-layer (Pt_{ASL}) structures with 100% metal dispersion and precisely controlled local coordination environment (embedded vs adsorbed) derived from Pt single-atoms (Pt₁) on ceria-alumina supports. The local coordination environment of Pt₁ not only governs its catalytic activity but also determines the Pt₁ structure evolution upon reduction activation. For CO oxidation, the highest turnover frequency can be achieved on the embedded Pt_{ASL} in the CeO₂ lattice, which is 3.5 times of that on the adsorbed Pt_{ASL} on the CeO₂ surface and 10–70 times of that on Pt₁. The favorable CO adsorption on



embedded Pt_{ASL} and improved activation/reactivity of lattice oxygen within CeO₂ effectively facilitate the CO oxidation. This work provides new insights for the precise control of the local coordination structure of active metal sites for achieving 100% atomic utilization efficiency and optimal intrinsic catalytic activity for targeted reactions simultaneously.

■ INTRODUCTION

Atomically dispersed metal catalysts offer great benefits in catalysis with near 100% utilization efficiency of the supported metals, especially for high-cost noble metals. As an emergent material system in heterogeneous catalysis, supported metal single-atom catalysts (SACs) have been well investigated in the last decade with broad applications. The intrinsic catalytic activity of SACs is highly determined by the local coordination structure of the isolated metal atoms. However, the precise control of the coordination structure of metal atoms in SACs is still a great challenge, and achieving superior intrinsic activity of SACs in certain reactions such as low-temperature CO oxidation is sometimes difficult because of the over-rigid local structure and complete isolation of active sites lacking synergistic effects from neighboring metal atoms. S,21–23

Recently, it has been demonstrated that the metal atomic single-layer (ASL) structures or the so-called metal rafts can be built on defective supports, which can maintain 100% metal utilization efficiency and at the same time possess active sites with neighboring metal atoms showing a synergistic effect, thus exhibiting exceptional advantages in wide catalytic applications. Other than the direct synthesis of two-dimensional (2D) rafts on certain supports, the post-reduction of metal single-atoms has been proven as another efficient approach to fabricate metal ASL structures. Provided that the precise control of post-reduction in H₂ flow, Pt ensembles on Pt

monolayer structures³³ can be obtained from Pt single-atoms supported on CeO2, which show much higher CO oxidation activity than the initial Pt SACs. Although ASL structures for metals such as Pt have been successfully created on several supports, as far as we know, these structures are usually present on the support surface showing relatively weak interaction with the support lattice matrix. It has been reported that the local structure of metal sites essentially determines the performance of supported metal catalysts, not only for metal single-atom sites but also for metal cluster sites. ^{26,34–36} For the case of metal ASL sites, however, whether the local coordination structure will impact their catalytic performance is still unclear and barely reported. Furthermore, taking the Pt case as an example, if the ASL sites are derived from post-reduction of SACs, whether the initial coordination structure of Pt singleatoms can determine the ultimate local structure of Pt ASL sites thus influencing the intrinsic catalytic activity requires systematic investigation. To answer these questions, in this work, we show the precise control of local coordination

Received: August 21, 2022



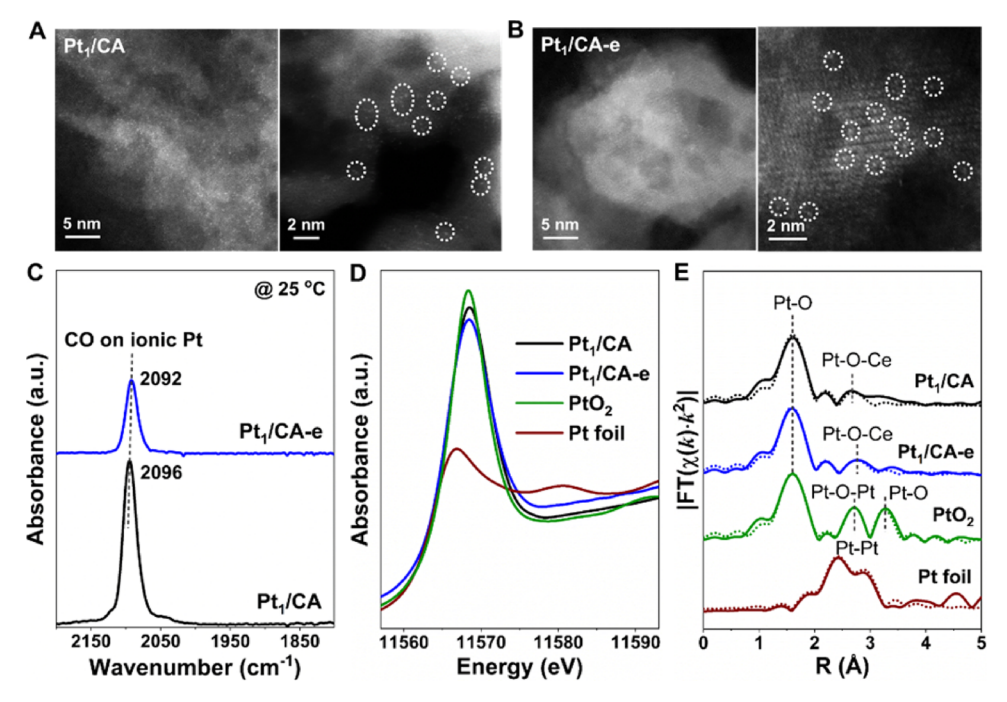


Figure 1. Structural characterization of Pt SACs. (A, B) High-angle annular dark field (HAADF) aberration-correction scanning transmission electron microscopy (AC-STEM) images and (C) in situ diffuse reflectance infrared Fourier transform spectroscopy (DRIFTS) of CO adsorption on Pt_1/CA and Pt_1/CA -e catalysts; (D) normalized Pt L_3 -edge X-ray absorption near edge structure (XANES) and (E) Fourier-transformed k^2 -weighted extended X-ray absorption fine structure (EXAFS) oscillations in R space for the Pt L_3 -edge in Pt_1/CA and Pt_1/CA -e catalysts (solid line: experimental data; dotted line: fitted data).

structures of Pt ASL sites derived from Pt single-atoms on CeO_2 and systematically study their intrinsic catalytic behavior in the CO oxidation reaction.

Herein, with defect enrichment on a CeO₂-Al₂O₃ support, we report the successful fabrication of Pt single-atom (Pt_1) , Pt atomic single-layer (Pt_{ASL}), and Pt multilayer cluster (Pt_C) catalysts with all or partial Pt atoms embedded in the CeO2 surface lattice. Based on systematic experimental studies and density functional theory (DFT) calculations, it is clearly revealed that the local coordination structure of Pt₁ sites not only determines the activity of Pt SACs but also governs their structural evolution for the formation of more active Pt_{ASI} and Pt_C structures. The embedded Pt_{ASL} sites with Pt atoms substituting Ce cations in the CeO2 surface lattice show the highest activity in CO oxidation reaction, far exceeding the surface-adsorbed Pt_{ASL} sites and the surface-adsorbed and lattice-embedded Pt_C or Pt₁ sites. A low overall activation energy for the reaction between active CO species adsorbed on embedded Pt_{ASL} sites and active interfacial oxygen species significantly contribute to the superior activity of embedded Pt_{ASL} structures fabricated on CeO₂.

■ RESULTS AND DISCUSSION

Defect Enrichment on Ceria-Alumina Support. A CeO₂/Al₂O₃ support with 30 wt % CeO₂ loading (CA) was prepared via the incipient wetness impregnation method and used for defect enrichment through H₂ reduction treatment. To achieve an optimal reduction temperature for defect enrichment on CA, the CA support was reduced at different temperatures (*i.e.*, 550, 750, and 850 °C, determined by H₂-temperature programmed reduction (H₂-TPR) result (Figure S1)) and loaded with 1 wt % Pt for CO oxidation testing after activation (Figure S2). The optimal defect enrichment condition on CA was confirmed as reduction in 10% H₂/Ar

at 750 °C for 2 h based on the highest CO oxidation performance achieved. Accordingly, the CA support and 1.0Pt/ CA catalyst with defect enrichment were fabricated using this optimal condition and designated as CA-HD and 1.0Pt/CA-HD (HD denotes 'high density' defects). It was noticed that the 1.0Pt/CA-HD catalyst with less CeO₂ usage consistently showed higher CO oxidation activity and catalytic stability than the conventional 1.0Pt/CeO₂ catalyst after reduction activation (Figure S3), suggesting its great potential in practical application. Compared to CA, a significant expansion in the crystal structure of CeO₂ was observed in CA-HD (Figures S4 and S5), indicating the formation of rich defects induced by H₂ reduction. Raman spectra (Figure S6B) and X-ray photoelectron spectroscopy (Figure S6C) results clearly confirmed that CA-HD had a much higher density of surface defects (mainly oxygen vacancies) than CA, because much more surface Ce3+ species and abundant peroxide species in the vicinity of Ce³⁺ cations were observed for CA-HD. 37-39 In contrast to the CA support with typical yellowish color, the CA-HD support showed grayish blue color because of the presence of rich defects, and such a defective support could be stable in the ambient atmosphere for more than 6 months without changing color (Figure S6A).

Impact of Defect Enrichment on the Local Structure of Pt Single-Atoms. Pt catalysts with 0.25 wt % Pt showing Pt₁ only species were fabricated on both CA and CA-HD supports, which was verified by the AC-STEM results in Figures 1A,B and S7. Such Pt₁ only catalysts can be designated as Pt₁/CA and Pt₁/CA-e (-e denotes 'embedded' Pt species on CA-HD). The *in situ* DRIFTS of CO adsorption (Figure 1C) showed that only linearly adsorbed CO on Pt₁ sites was present on Pt₁/CA (2096 cm⁻¹) and Pt₁/CA-e (2092 cm⁻¹). XANES results showed that the Pt species within Pt₁/CA and Pt₁/CA-e were in oxidized states which were close to that

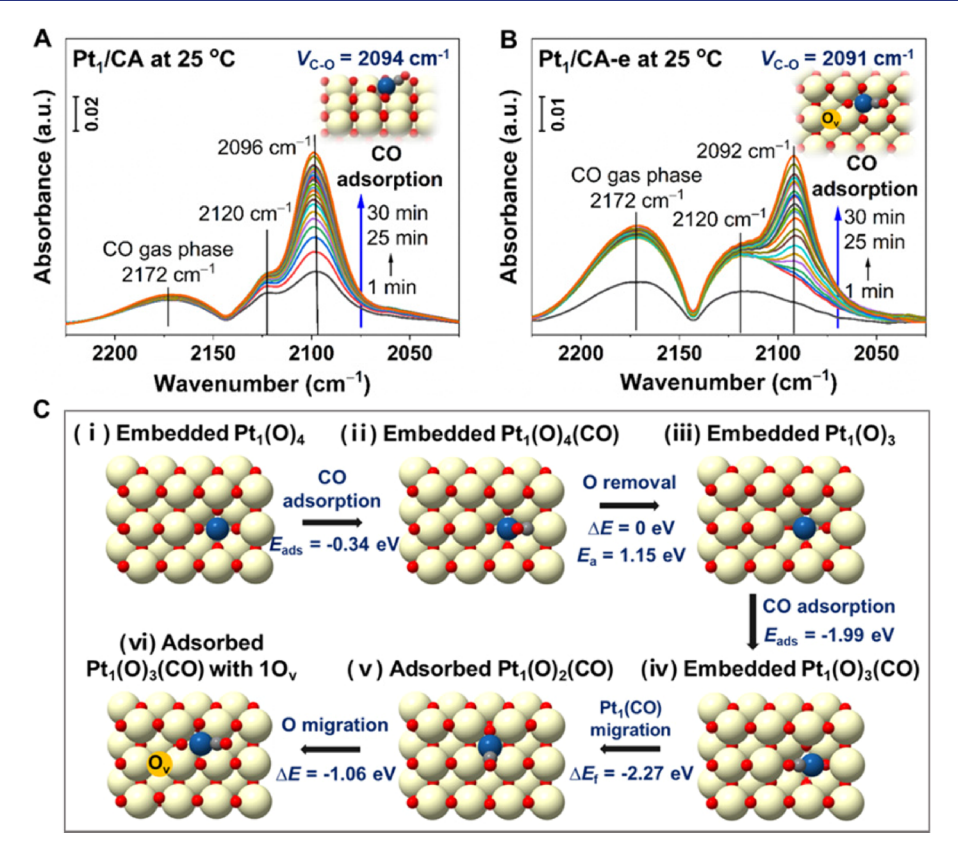


Figure 2. Time-resolved CO adsorption and theoretical calculations of Pt_1 structures after CO adsorption. In situ DRIFTS of CO adsorption as a function of exposure time in CO flow on (A) Pt_1/CA and (B) Pt_1/CA -e; as well as (C) simulated structure evolution process of Pt_1 within the Pt_1/CA -e catalyst during CO adsorption. Color code: Ce (yellow), O (red), and Pt (blue).

within PtO_2 (Figure 1D), and EXAFS results confirmed the absence of either Pt–Pt metallic bonds or Pt–O–Pt bonds and the exclusive presence of Pt–O and Pt–O–Ce bonds attributed to Pt₁ structures (Figure 1E). The XANES linear combination fitting (Figure S8 and Table S1) and EXAFS curve fitting (Table S2) suggested that the Pt₁ species within Pt₁/CA-e showed a lower average oxidation state (+3.3 vs+3.8), a slightly lower coordination number (CN) of Pt–O (3.8 vs 4.0), and a higher CN of Pt–O–Ce (1.7 vs 1.3) than those within Pt₁/CA. These results clearly demonstrated that the Pt species were present in a single-atom form in both Pt₁/CA and Pt₁/CA-e catalysts, but with different local coordination environments.

DFT calculations were performed to identify the Pt₁ structures on the O-terminated (100) surface of CeO₂ (Figure S9), which is equivalent to the observed CeO₂ (020) facet in AC-STEM results. Two Pt₁ structures, i.e., adsorbed Pt₁ and embedded Pt₁ on CeO₂ (100), were proposed to represent Pt₁/CA and Pt₁/CA-e, respectively. Similar to the result reported in the literature, 40 adsorbed Pt₁ within Pt₁/CA preferred to bond with four surface oxygens and formed a square-planar Pt₁(O)₄ structure (Figure S13A). However, on Pt₁/CA-e, Pt₁ was postulated to substitute a surface Ce cation on the CeO₂ (100). Because the CeO₂ (100) surface exposed 6-fold Ce cations, by substituting a Ce cation, the Pt₁ was surrounded by six oxygen anions. 41,42 However, as shown in Figure S11, the differential oxygen vacancy (O_v) formation energies by removing two top-layer oxygens between Pt1 and Ce (0.29 eV for the first oxygen removal and -0.61 eV for the second oxygen removal) were much lower than that on the CeO₂ (100) clean surface (1.46 eV for one oxygen removal,

Figure S10), indicating that the two top-layer oxygens on Pt_1/CA -e were unstable and could be readily removed. Therefore, a stable model structure with $Pt_1(O)_4$ embedded in the CeO_2 lattice matrix was constructed for the Pt_1/CA -e catalyst, as shown in Figure S13B. It was further verified that the Pt embedding into the defective CeO_2 by substituting a Ce site was more thermodynamically favorable than that into stoichiometric CeO_2 (Figure S12). The oxidation states of adsorbed Pt_1 (+2.6) and embedded Pt_1 (+2.1) on CeO_2 (100) were calculated, which suggested that the adsorbed Pt_1 was more positively charged than the embedded Pt_1 (Figure S13), consistent with the Pt L_3 -edge XANES fitting results (Table S1).

Figure 2A,B shows the *in situ* DRIFTS of CO adsorption as a function of exposure time on Pt_1/CA and Pt_1/CA -e. Once exposed to CO, both the bands at 2096 and 2120 cm⁻¹ showed up and gradually increased for Pt_1/CA , suggesting the simultaneous and continuous adsorption of CO on Pt_1 sites. In contrast, on Pt_1/CA -e, the band at 2092 cm⁻¹ gradually appeared only after the CO physisorption on Pt_1 sites (2120 cm⁻¹)^{43,44} reached the saturation state, indicating that the CO chemisorption on embedded Pt_1 could only occur once the Pt_1 sites were altered by the physisorbed CO. Furthermore, a redshift of the CO vibrational peak and lower CO adsorption intensity were observed for Pt_1/CA -e (2092 cm⁻¹) compared to that on Pt_1/CA (2096 cm⁻¹), suggesting again the different local structures of Pt single-atoms within Pt_1/CA and Pt_1/CA -e catalysts.

To further confirm the local structures of Pt_1 species within Pt_1/CA and Pt_1/CA -e as proposed above, DFT calculations of CO adsorption onto the surface-adsorbed $Pt_1(O)_4$ structure

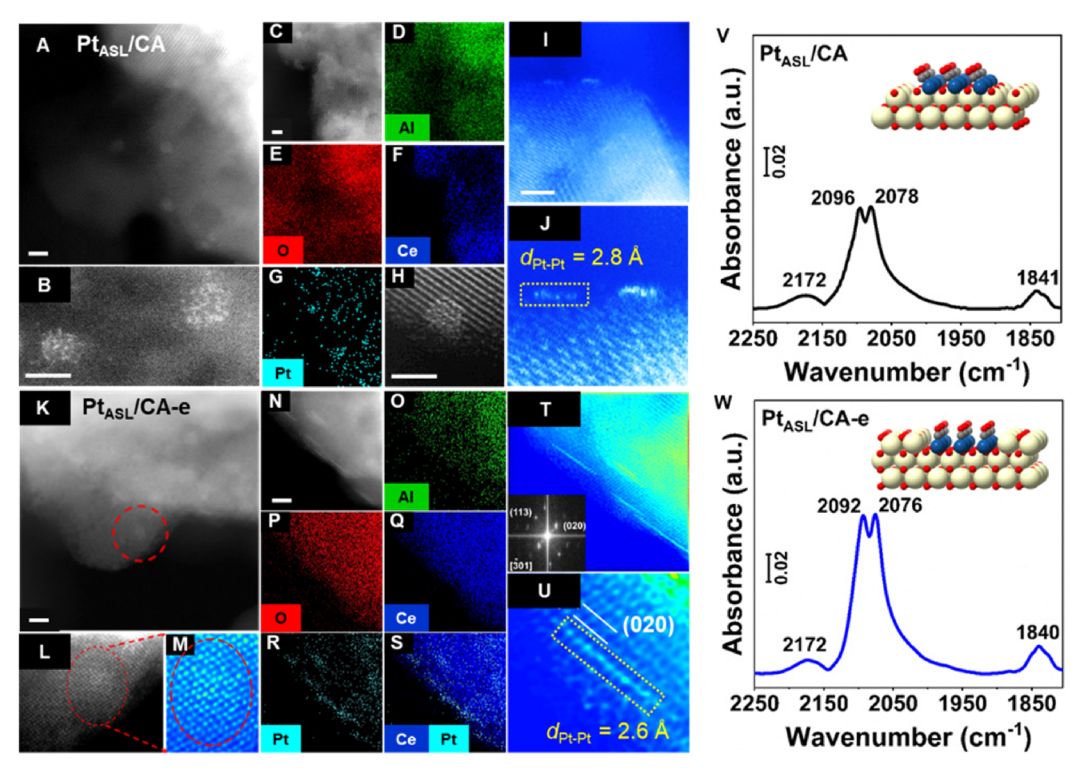


Figure 3. Structural characterization of Pt atomic single-layer catalysts. HAADF AC-STEM images and EDS mapping results (with scale bars as 2 nm) for (A–J) Pt_{ASL}/CA and (K–U) Pt_{ASL}/CA -e, and in situ DRIFTS of CO adsorption on (V) Pt_{ASL}/CA and (W) Pt_{ASL}/CA -e in CO flow at 25 °C (the models of Pt_{ASL}/CA and Pt_{ASL}/CA -e with adsorbed CO are shown as inserted in V and W).

and the embedded Pt₁(O)₄ structure on CeO₂ (100) were conducted. As shown in Figure S14, for the surface-adsorbed Pt₁(O)₄ structure within Pt₁/CA, the CO adsorption could lead to the formation of adsorbed $Pt_1(O)_3(CO)$ structure with the calculated CO wavenumber as 2094 cm⁻¹, which was very close to the experimental measurement (2096 cm⁻¹) in this study. As illustrated in Figure 2B, the CO adsorption on Pt₁ within Pt₁/CA-e occurred only after the Pt₁ sites being saturated by physisorbed CO, indicating the possible structural evolution of embedded Pt₁ in the CO flow. Figure 2C shows the simulation results for this structural evolution. Without an additional oxygen vacancy near Pt1, only CO physisorption $(E_{\text{ads}} = -0.34 \text{ eV})$ could be achieved on the embedded $Pt_1(O)_4$ structure, as observed in experiment. However, once an oxygen in the embedded $Pt_1(O)_4$ structure was slowly removed by the physisorbed CO ($\Delta E = 0$ eV, $E_a = 1.15$ eV), strong CO chemisorption ($E_{ads} = -1.99 \text{ eV}$) on Pt_1 could occur. Accordingly, the two Pt₁-O bonds could break easily after the CO chemisorption, which made the Pt₁ weakly bonded and diffusible (structure iv in Figure 2C). With the favorable diffusion of the Pt₁(CO) moiety and a nearby surface oxygen atom, eventually, a stable, adsorbed Pt₁(O)₃(CO) structure with a nearby surface O_v (structure vi in Figure 2C) was obtained with a calculated CO wavenumber of 2091 cm⁻¹, which was consistent with our experimental measurement (2092 cm⁻¹) and the result reported in the literature. ¹⁹ In CO flow, the CO adsorption energies on the stable Pt₁ structures within Pt₁/CA and Pt₁/CA-e were calculated as -2.71 and -2.52 eV (Table S3), respectively. Compared to the facile CO chemisorption on the surface-adsorbed Pt₁(O)₄ structure, the reaction barrier ($E_a = 1.15 \text{ eV}$) required and relatively lower CO adsorption energy (-2.52 eV) on the embedded $Pt_1(O)_4$ structure well explained the lower CO adsorption intensity on

 Pt_1/CA -e than on Pt_1/CA as observed in experiments (Figures 1C and 2A,B). Therefore, complementary methods confirmed that distinct local coordination environments for Pt_1 species were indeed present on Pt_1/CA and Pt_1/CA -e, which were the surface-adsorbed $Pt_1(O)_4$ structure on regular CeO_2 (100) and embedded $Pt_1(O)_4$ structure on CeO_2 (100) with enriched defects, respectively.

Creating Pt Atomic Single-Layer Structures for More **Efficient CO Oxidation.** Reduction activation can be used to create more active Pt sites from Pt₁ species on CeO₂ for CO oxidation. 22,45,46 By fine-tuning the H₂ reduction conditions, the most active Pt sites on CA and CA-HD supports for CO oxidation were successfully fabricated using Pt₁/CA and Pt₁/ CA-e as precursor catalysts (Figure S15). The most active Pt sites on both supports have been confirmed as Pt atomic single-layer structures (Pt_{ASL}) located on CeO₂ (020) with 100% Pt dispersion by the AC-STEM technique (Figure 3A-U). For the activated catalyst derived from Pt₁/CA, the Pt_{ASL} structures were observed as the surface-adsorbed state on CeO₂ (Figure 3I,J) with the distance for Pt-Pt (d_{Pt-Pt}) as ca. 2.8 Å (Figure 3J) and average size as ca. 1.5 nm (Figure S16A), showing no clear lattice matching between Pt and CeO₂ (denoted as Pt_{ASL}/CA). However, for the activated catalyst derived from Pt₁/CA-e, the Pt_{ASL} structures were obviously embedded in the CeO₂ lattice substituting Ce atoms (Figure 3T,U) with the d_{Pt-Pt} as ca. 2.6 Å (Figure 3U) and average size as ca. 1.4 nm (Figure S16B), showing perfect crystal plane matching between Pt and CeO₂ (denoted as Pt_{ASL}/CA-e). When deeper reduction at higher temperature (e.g., 500 °C) was applied on Pt₁/CA and Pt₁/CA-e catalysts, the adsorbed Pt_C structure within Pt_C/CA and embedded Pt_C structure within Pt_C/CA-e were clearly observed (Figure S17), respectively. In summary, the distinct local coordination

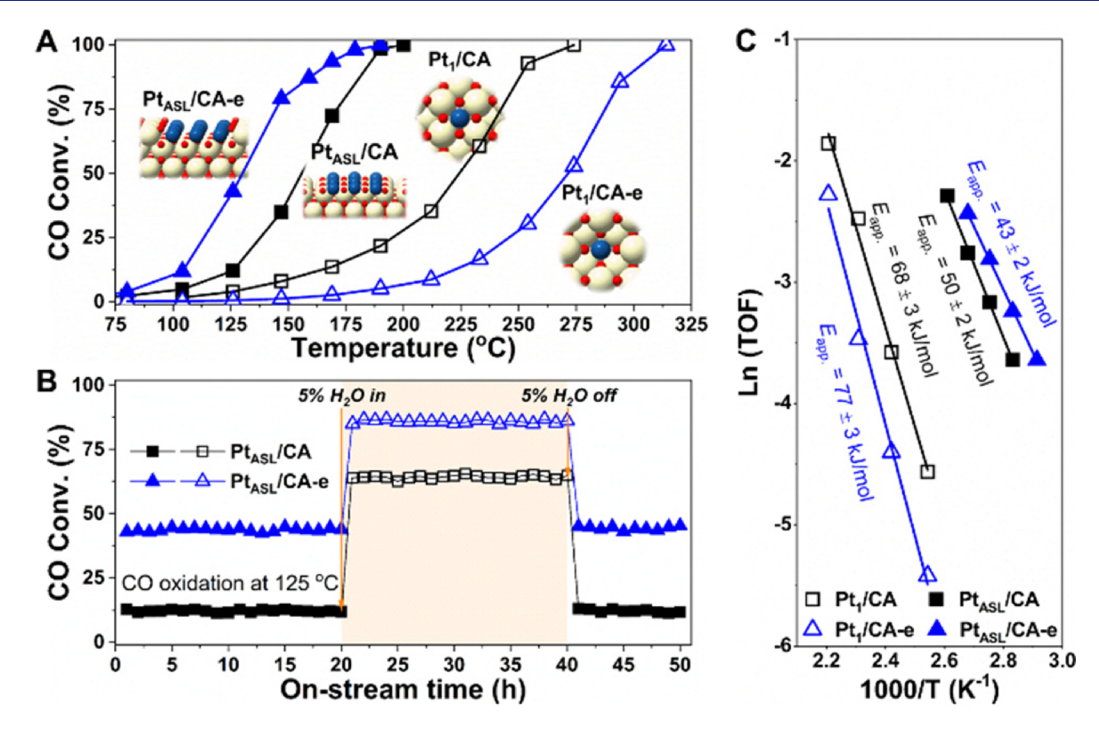


Figure 4. Catalytic performance measurements. CO oxidation activity on (A) Pt/CA catalysts with different Pt structures and (B) Pt_{ASL}/CA and Pt_{ASL}/CA-e catalysts with H₂O in feedstock, and (C) Arrhenius plots and apparent activation energy $(E_{app.})$ values for CO oxidation on Pt/CA catalysts with different Pt structures. Reaction condition: Steady-state testing, $[CO] = [O_2] = 1\%$, $[H_2O] = 5\%$ (if used), balanced with Ar, with WHSV of 200,000 mL· g_{cat}^{-1} · h^{-1} .

structures of Pt_1 on CA and CA-HD determined the different Pt_1 structural evolution processes during reduction activation, obtaining the adsorbed Pt_{ASL} and Pt_C structures on CA and the embedded Pt_{ASL} and Pt_C structures on CA-HD.

As verified by the in situ DRIFTS results (Figure 3V,W), a similar CO adsorption behavior was observed on Pt_{ASI}/CA and Pt_{ASL}/CA-e catalysts. The CO species linearly (2078 and 2076 cm^{-1}) and bridging (1841 and 1840 cm⁻¹) adsorbed on Pt atoms within Pt_{ASL} structures were clearly observed, agreeing well with the observation of CO adsorption on Pt-O-Pt ensembles as reported by Wang et al.²² The presence of linearly adsorbed CO species (2096 and 2092 cm⁻¹) suggested that there was still a portion of Pt single atoms remaining within both catalysts after reduction activation. The XANES and EXAFS of Pt L₃-edge were also measured to elucidate the oxidation states and local structures of Pt species within Pt_{ASL}/ CA and Pt_{ASL}/CA-e catalysts (Figure S18). As determined by XANES fitting results (Table S1 and Figure S19), Pt_{ASL}/CA-e showed a lower oxidation state of Pt_{ASL} species (+2.0) compared to Pt_{ASL}/CA (+2.4). As shown by EXAFS fitting results (Table S2 and Figure S18B), besides Pt-O and Pt-O-Ce bonds, the Pt-O-Pt bonds could also be observed in both catalysts, suggesting the presence of neighboring Pt atoms connected by oxygen atoms within the Pt_{ASL} structures. Such Pt_{ASL} structures with a synergistic effect from neighboring Pt atoms might benefit the adsorption of active CO species under CO oxidation conditions. Compared to Pt_{ASL}/CA, Pt_{ASL}/CA-e showed shorter bond lengths of Pt-O-Ce and Pt-O-Pt and a slightly higher CN of Pt-O-Ce because of its unique embedded Pt_{ASL} structure in CeO₂.

To simulate the embedded Pt_{ASL} structure within Pt_{ASL}/CA -e, a periodic Pt single layer (containing nine Pt atoms) on CeO_2 (100) was constructed by substituting surface Ce cations. After removing the top-layer unstable O anions in Pt-

O-Pt (with the O_v formation energy as ~ -0.1 eV) (Figure S20), the O anions in Pt-O-Ce on the top layer preferred to diffuse to the bridge sites of interfacial Ce cations with a high exothermicity of 5.15 eV (Figure S21). Therefore, the representative model structure for Pt_{ASL}/CA-e was constructed, in which each Pt cation was surrounded by four oxygens on CeO₂ (100). In this structure with 100% Pt dispersion, there was no Pt-Pt direct interaction in the first coordination shell of Pt (Figure S22B) with the Pt-Pt distance of 3.8 Å. Based on AC-STEM and in situ DRIFTS results (Figure 3), Pt_{ASL}/CA showed high similarity to Pt_{ASL}/CA-e except that the Pt_{ASL} structure was adsorbed on the surface of CeO_2 in the former. Therefore, analogous to $\mathrm{Pt}_{\mathrm{ASL}}/\mathrm{CA}\text{-e},$ a model structure for Pt_{ASL}/CA was created on the CeO₂ (100) surface (Figure S22A). In this surface-adsorbed Pt_{ASL} structure, the Pt-Pt distance of 4.1 Å was slightly longer than that in the embedded Pt_{ASL} structure, which was consistent with the observation from STEM images and EXAFS results.

On Pt_{ASL}/CA and Pt_{ASL}/CA -e catalysts, the calculated CO adsorption energies (Figure S23 and Table S3) indicated that both Pt_{ASL} structures favored high CO coverage. It is noteworthy that the calculated average CO adsorption energy on embedded Pt_{ASL} within Pt_{ASL}/CA -e (-1.38 eV) was much lower than that on adsorbed Pt_{ASL} within Pt_{ASL}/CA (-2.01 eV), embedded Pt_{ASL} within Pt_{ASL}/CA -e (-2.52 eV), and adsorbed Pt_{ASL} within Pt_{ASL}/CA (-2.71 eV). The *in situ* DRIFTS of CO desorption was also performed to verify the CO adsorption ability on Pt_{ASL} structures. As shown in Figure S24, the decline degree of the CO peak areas as a function of desorption temperature on all catalysts (Pt_{ASL}/CA -e > Pt_{ASL}/CA -e oddsorption energies. According to the Sabatier principle, 47 the Pt-CO bonding on the Pt_{ASL}/CA -e

Table 1. TOF, Apparent Activation Energy $(E_{app.})$, and Reaction Orders for CO and O₂ in CO Oxidation on Different Pt/CA Catalysts

					reaction order ^c	
sample	Pt dispersion (%) ^a	active sites	TOF at 125 $^{\circ}$ C $(\times 10^{-2} \text{ s}^{-1})$	$\frac{E_{\mathrm{app.}}}{(\mathrm{kJ/mol})^{b}}$	СО	O ₂
Pt ₁ /CA	100	isolated Pt ₁ adsorbed on the CeO ₂ surface	7.8	68 ± 3	0.48	-0.02
Pt ₁ /CA-e	100	isolated Pt ₁ embedded in the CeO ₂ lattice substituting Ce cations	1.2	77 ± 3	0.79	0.05
Pt_{ASL}/CA	100	adsorbed Pt atomic single-layer structure on the CeO ₂ surface	23.8	50 ± 2	0.00	0.00
$\mathrm{Pt}_{\mathrm{ASL}}/\mathrm{CA}$ -e	100	embedded Pt atomic single-layer structure in the ${\rm CeO_2}$ lattice with Pt cations substituting Ce cations	84.0	43 ± 2	0.05	0.01

"Based on spectroscopic observations from HAADF AC-STEM images. ^bThe $E_{app.}$ values were calculated with CO conversions below 8% (under a WHSV of 200,000 or 400,000 mL· g_{cat}^{-1} ·h⁻¹). ^cThe reaction orders were measured with CO conversions below 10% (under a WHSV of 200,000 mL· g_{cat}^{-1} ·h⁻¹).

catalyst was neither too strong nor too weak, which would benefit its CO oxidation performance.

The DFT calculations of O_v formation energies (Eo_v) for four types of oxygen species including terrace $O(O_I)$, interface O (O $_{II}$), O in Pt-O-Ce (O $_{III}$), and Pt-O-Pt (O $_{IV}$) were performed to further probe the stable Pt structures and the reactivity of oxygen species within Pt_{ASL}/CA and Pt_{ASL}/CA-e catalysts (Figure S25). As listed in Table S4, with the full coverage of CO on Pt_{ASL} structures, the Eo_v values of the four types of oxygen species (O_I, O_{II}, O_{III}, O_{IV}) were calculated as 2.52, 2.01, 2.99, and 0.75 eV for Pt_{ASL}/CA , respectively, and as -0.85, -0.68, 1.84, and 1.37 eV for Pt_{ASL}/CA -e, respectively. Because the oxygen species on Pt_{ASL}/CA were stable enough, the adsorbed Pt_{ASL} structure fully covered by CO was expected to be stable in the CO flow at 25 °C and therefore was adopted as the starting structure to study the CO oxidation mechanism on Pt_{ASL}/CA (Figure S27A). Because of the low Eo_v of terrace O (-0.85 eV) and interface O (-0.68 eV) in Pt_{ASL}/CA-e, these two types of oxygen species were highly reactive and readily removed in the CO flow. Via regulating the distribution of oxygen vacancies (Figure S26), the most stable structure of embedded Pt_{ASL} with two terrace O_v on CeO₂ could be obtained after structure relaxation under CO adsorption or reaction condition, which was used as the starting structure of Pt_{ASL}/CA-e (Figure S27B) for the CO oxidation mechanism study. On the stable structures of adsorbed Pt_{ASL} and embedded Pt_{ASL} with two terrace O_v on CeO₂ (Figure S27), the calculated wavenumbers of CO linearly chemisorbed on the Pt atoms within Pt_{ASL} were 2069 and 2066 cm⁻¹, respectively, which were in line with the vibrational frequency sequence of experimental CO adsorption bands observed on $Pt_{ASL}/CA (2078 \text{ cm}^{-1}) \text{ and } Pt_{ASL}/CA-e (2076 \text{ cm}^{-1}) \text{ at } 25 \text{ }^{\circ}C$ (Figure 3).

Figure 4A shows the CO oxidation activity on Pt₁/CA, Pt₁/CA-e, Pt_{ASL}/CA, and Pt_{ASL}/CA-e catalysts with different Pt structures (adsorbed and embedded Pt₁ or Pt_{ASL}). Pt₁/CA showed higher catalytic activity than Pt₁/CA-e, with lower light-off temperature achieved on Pt₁/CA with T50 (the temperature corresponding to 50% of CO conversion) as 223 °C compared to that on Pt₁/CA-e (with T50 as 271 °C). The weak bonding of CO on the embedded Pt₁(O)₄ structure on CeO₂ (100) should be the main reason for the low CO oxidation activity of Pt₁/CA-e. After activation, both Pt_{ASL}/CA and Pt_{ASL}/CA-e catalysts with Pt_{ASL} structures exhibited much higher CO oxidation activity than their corresponding Pt₁ precursor catalysts. As expected, the Pt_{ASL}/CA-e catalyst significantly outperformed the Pt_{ASL}/CA catalyst for CO oxidation, with much lower T50 achieved on the former

(130 °C) than on the latter (156 °C). At 125 °C, as shown in Table 1, the turnover frequency (TOF) of CO on Pt_{ASL}/CA-e $(84.0 \times 10^{-2} \text{ s}^{-1})$ was 70 times of that on Pt₁/CA-e (1.2 × 10^{-2} s^{-1}), 10 times of that on Pt₁/CA (7.8 × 10^{-2} s^{-1}), and 3.5 times of that on Pt_{ASI}/CA (23.8 \times 10⁻² s⁻¹). It should be pointed out that the TOFs for CO oxidation on Pt₁/CA, Pt₁/ CA-e, and Pt_{ASL}/CA in this study were within the same order of magnitude as those on the reported Pt SACs^{12,19,32,49,50} and Pt 2D ensemble or raft catalysts 22,32 on CeO2-based supports (Table S5). In agreement with the conclusion that water vapor could benefit the CO oxidation on Pt-CeO2-based catalysts, ^{22,49,51} a reversible positive effect of H₂O on CO conversion was also observed on Pt_{ASL}/CA and Pt_{ASL}/CA-e (Figure 4B). With 5% H₂O in the feed stream, the Pt_{ASI}/CA-e catalyst still exhibited much higher CO oxidation activity than Pt_{ASL}/CA (Figures 4B and S28). Kinetics measurements revealed that the apparent activation energy $(E_{app.})$ for CO oxidation on these catalysts decreased in the order of Pt₁/CA-e $(77 \pm 3 \text{ kJ/mol}) > \text{Pt}_1/\text{CA} (68 \pm 3 \text{ kJ/mol}) > \text{Pt}_{ASI}/\text{CA} (50 \pm$ 2 kJ/mol) > Pt_{ASL}/CA-e (43 ± 2 kJ/mol) (Figure 4C and Table 1), suggesting again that the embedded Pt atomic singlelayer structure on CeO2 was the most active Pt site for CO oxidation. Furthermore, the embedded Pt_{ASL}/CA-e catalyst showed a much higher TOF for CO oxidation than other Pt-CeO₂-based catalysts containing different types of Pt sites. Because of its superior catalytic stability and water tolerance, the Pt_{ASI}/CA-e catalyst shows great potential in practical applications such as vehicle emission control although it cannot surpass most Au-CeO₂-based catalysts with lower $E_{\text{app.}}$ (< 30 kJ/mol) and light-off temperatures for CO oxidation (Table S5). $^{52-54}$

Identification of Active Oxygen and CO Species on Pt Atomic Single-Layer Structures in CO Oxidation. To determine the roles of CO and O2 in the CO oxidation reaction, the reaction orders of CO and O2 on different catalysts were measured (Figure S29). The CO reaction orders on Pt₁/CA and Pt₁/CA-e were determined as 0.48 and 0.79 (Figure S29A, Table 1), respectively. The O₂ reaction orders on Pt₁/CA and Pt₁/CA-e were dependent on the O₂/CO ratio, which were -0.02 and 0.05, respectively, when the O_2/CO ratio was below 1, and were 0.32 and 0.25, respectively, when the O_2/CO ratio was above 1 (Figure S29B). Under the activity testing condition in this study $(O_2/CO \le 1.0)$, the CO oxidation rates on Pt₁/CA and Pt₁/CA-e could be expressed as $r(Pt_1/CA) = k_1 \cdot [CO]^{0.48} \cdot and r(Pt_1/CA-e) = k_2 \cdot [CO]^{0.79}$ respectively (k_1 and k_2 are constants). Similar to the results reported for Pt₁ catalysts in the literature, 19,48 the CO oxidation reaction rates on Pt₁/CA and Pt₁/CA-e were mainly

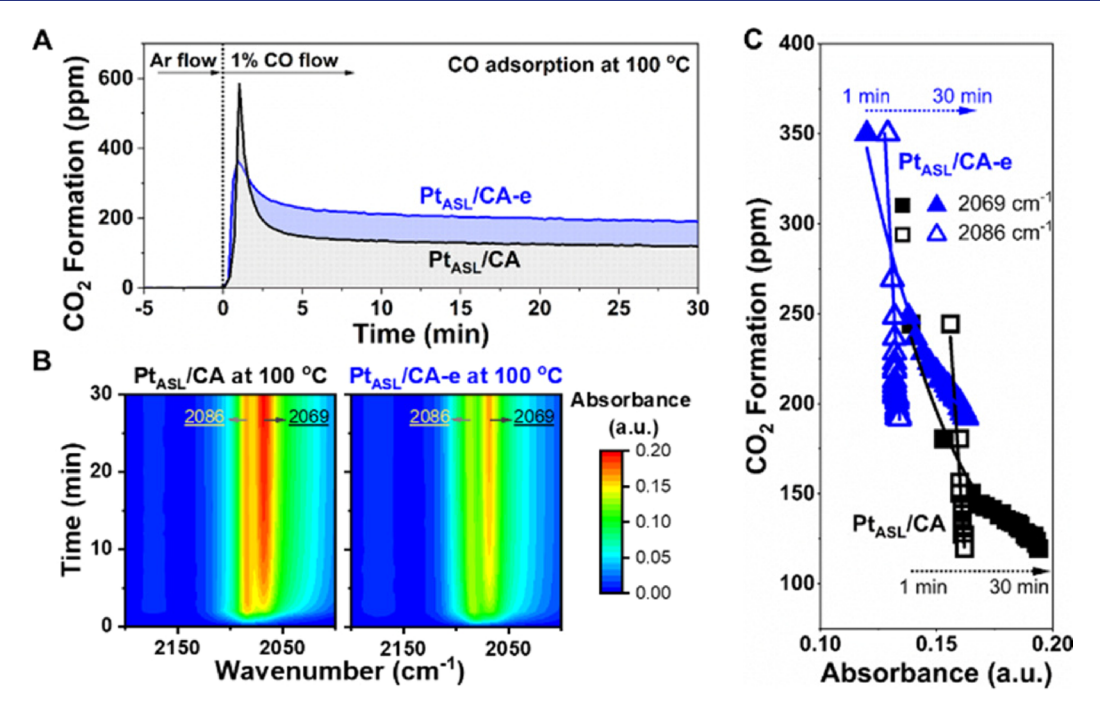


Figure 5. Measurements on active oxygen species. Time-resolved (A) CO_2 formation after exposure to continuous CO flow and (B) in situ DRIFTS of CO adsorption (in CO flow only), and (C) CO_2 formation as a function of CO adsorption intensity resulting from the reaction between CO and oxygen species within Pt_{ASL}/CA and Pt_{ASL}/CA -e catalysts.

determined by CO adsorption. The lower CO reaction order measured on Pt_1/CA (0.48) than on Pt_1/CA -e (0.79) suggested that the former catalyst was more favorable for CO adsorption. As confirmed by DFT calculations (Table S3) and in situ DRIFTS results (Figures 2 and S24), the relatively stronger and more favorable CO adsorption on the surfaceadsorbed Pt₁ sites than that on the lattice-embedded Pt₁ sites could contribute to the higher CO oxidation activity achieved on Pt₁/CA than on Pt₁/CA-e. This was also confirmed by an in situ DRIFTS study coupled with mass spectrometry (MS) to monitor the CO reacting with oxygen species within Pt₁/CA and Pt₁/CA-e catalysts at 100 °C (Figure S30), during which a much more intense and faster saturation of CO adsorption could be achieved on Pt₁/CA than on Pt₁/CA-e (Figure S30A). Similar to the sequence of CO oxidation activity, during the whole interaction process between CO and Pt₁ catalysts, Pt₁/CA exhibited much higher CO₂ formation than Pt₁/CA-e (Figure S30B). Different from the case for Pt₁/CA in which a slight decrease of CO₂ formation was observed as the CO adsorption enhanced, for Pt₁/CA-e, a continuous and significant increase of CO₂ formation was observed with the increase of CO adsorption (Figure S30C). Although the initial oxygen mobility was observed lower on Pt₁/CA-e than on Pt₁/ CA (Figure S31), as illustrated in Figure 2C, more oxygen vacancies could be generated on Pt₁/CA-e along the CO adsorption, which could benefit the oxygen mobility and improve its CO oxidation efficiency to a certain extent.

The reaction orders for CO and O_2 in CO oxidation on Pt_{ASL}/CA and Pt_{ASL}/CA -e catalysts were also measured (Figure S29C,D), which were both almost 0. The CO oxidation rates on both Pt_{ASL}/CA and Pt_{ASL}/CA -e catalysts depended on the partial pressures of neither CO nor O_2 , indicating that there was no competitive adsorption between CO and O_2 because they should have different adsorption sites. Similar to previous reports on $Pt-CeO_2$ -based catalysts, 49,55,56 the CO oxidation on Pt_{ASL}/CA and Pt_{ASL}/CA

CA-e followed the Mars-van Krevelen (MvK) mechanism, in which the CO adsorbed on Pt_{ASL} sites could react with lattice oxygen from CeO_2 or Pt-O-Pt. In addition, compared to the positive reaction order for CO on Pt_1 sites, the zero-reaction order for CO on Pt_{ASL} sites indicated again that the Pt_{ASL} sites were more beneficial for CO adsorption.

To determine the active oxygen species and better understand the advantages of embedded PtASL over adsorbed Pt_{ASL}, the in situ DRIFTS study coupled with MS to monitor the CO reacting with oxygen species within Pt_{ASL}/CA and Pt_{ASL}/CA-e catalysts was also performed at 100 °C. Compared to an intense CO₂ formation peak observed on Pt_{ASL}/CA in the first 2 min, a lower CO₂ formation peak was observed on Pt_{ASL}/CA-e, suggesting that less surface oxygen species were present on Pt_{ASL}/CA-e (Figure 5A). As reported by Wang et al., the oxygen species in Pt-O-Pt ensembles on the CeO2 surface was more active than the lattice oxygen in CeO2. Similarly, in the case of Pt_{ASL}/CA, the oxygen species in the adsorbed Pt_{ASL} structure (O_{IV}) was also more reactive than the lattice oxygen in CeO₂ (O₁, O₁₁, and O₁₁₁), which was already verified by the DFT calculations as mentioned earlier (Figure S25A and Table S4). However, on Pt_{ASL}/CA, a sharp and immediate decline in CO2 formation was observed once the surface oxygen species in the adsorbed Pt_{ASL} structure was largely consumed. In clear contrast, although Pt_{ASL}/CA-e showed lower CO₂ formation initially because of the presence of less active surface oxygen species in embedded PtASL, it actually exhibited much higher CO2 formation than PtASL/CA as the CO adsorption time prolonged (e.g., above 2 min). Such results suggested that the lattice oxygen associated with the embedded Pt_{ASL} structure within Pt_{ASL}/CA-e was more reactive than that associated with the adsorbed Pt_{ASL} structure within Pt_{ASL}/CA. H₂-TPR results (Figure S32) also confirmed that much higher reactivity of lattice oxygen could be achieved on Pt_{ASL}/CA-e than on Pt_{ASL}/CA. The oxygen storage capacity (OSC) measurement (Figure S33) further demonstrated that

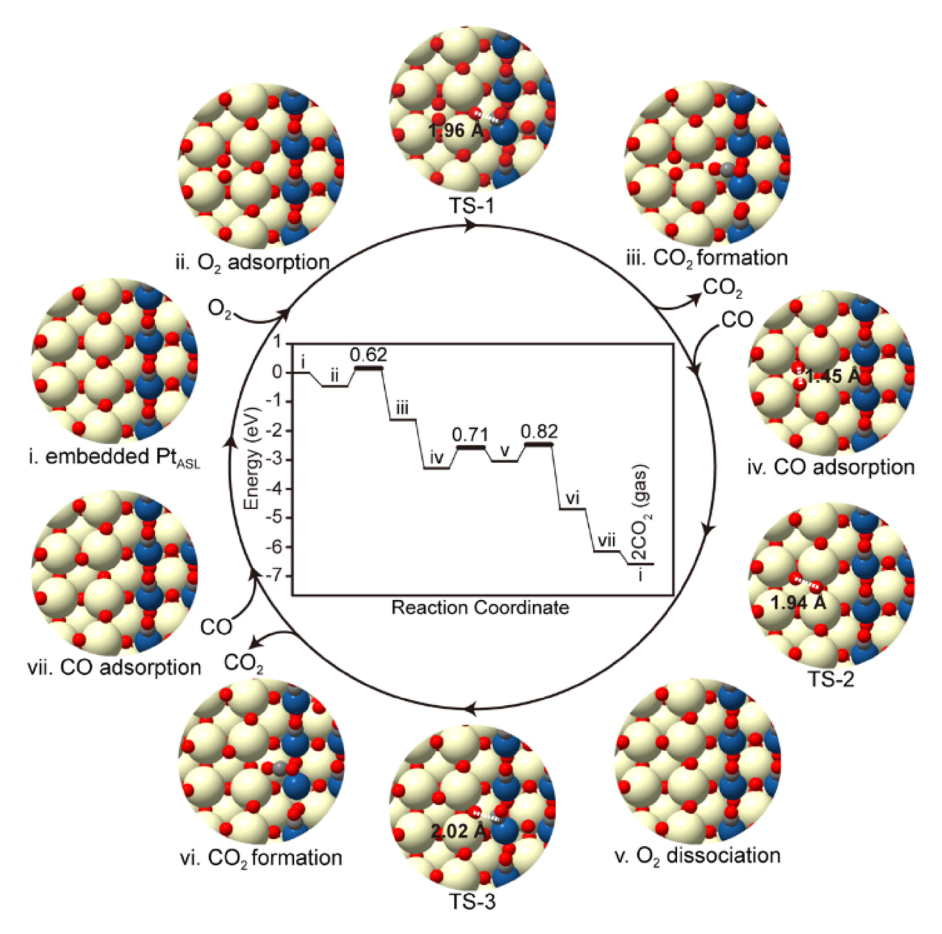


Figure 6. Potential energy diagrams and configurations for the CO oxidation cycle on the Pt_{ASL}/CA -e catalyst. The CO oxidation proceeded on an embedded Pt atomic single-layer unit in Pt_{ASL}/CA -e. The reaction energies and activation energies are indicated in eV in the potential energy diagram. Color code: Ce (yellow), O (red), Pt (blue), and C (gray). Corresponding energetics are given in Table S7.

 Pt_{ASL}/CA -e exhibited much better oxygen activation and transfer ability than Pt_{ASL}/CA . These experimental data were highly consistent with the DFT calculation results (Table S4), showing that the values for terrace O (O_I), interface O (O_{II}), and O in Pt–O–Ce (O_{II}) on Pt_{ASL}/CA-e were indeed much lower than those on Pt_{ASL}/CA. The unique embedded Pt_{ASL} structure could facilitate the activation of lattice oxygen in CeO₂ more efficiently, which contributed to the superior CO oxidation activity of the Pt_{ASL}/CA-e catalyst.

Figure 5B shows the accumulated CO adsorption bands on Pt_{ASL}/CA and $Pt_{ASL}/CA\text{-e}$ catalysts at 100 $^{\circ}C.$ As discussed above, the oxygen species within Pt-O-Pt could be consumed by CO at 100 °C; therefore, the Pt_{ASL} structures with in situ formed $\boldsymbol{O}_{\boldsymbol{v}}$ were created to represent the defective Pt_{ASL}/CA and Pt_{ASL}/CA-e catalysts under reaction conditions (Figure S34). With creating O_v in Pt_{ASL} model structures, the calculated CO adsorption frequency decreased from 2069 to 2063 cm⁻¹ on the adsorbed Pt_{ASL} structure and from 2066 to $2060~\text{cm}^{-1}$ on the embedded Pt_{ASL} structure. This was consistent with the experimental observation of CO adsorption frequency shifts on Pt_{ASL}/CA (from 2078 to 2069 cm⁻¹) and Pt_{ASL}/CA -e (from 2076 to 2069 cm⁻¹). In addition, the CO adsorption on residual Pt_1 sites (2086 cm⁻¹) was also observed. Figure 5C shows the relationship between CO₂ formation and CO adsorption intensity on different Pt sites within Pt_{ASL}/CA and Pt_{ASL}/CA-e catalysts upon flowing CO at 100 °C. An obvious increase of CO adsorption on Pt_{ASL} sites (2069 cm⁻¹) and no apparent change of CO adsorption at Pt₁

sites (2086 cm $^{-1}$) were observed on both catalysts along with the decrease of CO $_2$ formation. These results clearly suggested that the most reactive CO molecules adsorbed on both Pt_{ASL}/CA and Pt_{ASL}/CA-e catalysts should be those on Pt_{ASL} sites other than on Pt $_1$ sites. The *in situ* DRIFTS results of O $_2$ reacting with preadsorbed CO species on Pt $_1$ /CA-e and Pt_{ASL}/CA-e at 50 $^{\circ}$ C further confirmed that the CO species adsorbed on Pt $_1$ sites were indeed spectator species at low temperature, and the CO species adsorbed on Pt_{ASL} sites were truly reactive species participating in the CO oxidation (Figure S35).

CO Oxidation Cycle on Pt Atomic Single-Layer Structures. To better understand how the local structures of Pt_{ASL} influenced the CO oxidation performance, DFT calculations were conducted to reveal the CO oxidation mechanism on Pt_{ASL}/CA and Pt_{ASL}/CA-e catalysts. Starting from the adsorbed Pt_{ASL} structure with the full coverage of *CO (* represents the adsorbed state) (Figure S27A), as verified above in Table S4, the O in Pt-O-Pt (O_{IV} with Eo_v = 0.75 eV) was the most reactive oxygen species on Pt_{ASI}/CA, which was directly involved in the CO oxidation. As shown in Figure S36 and Table S6, the mechanism was initialized with *CO reacting with the O in Pt-O-Pt within adsorbed PtASL (structures i to ii), with an activation energy of 1.78 eV (TS-1). After CO₂ desorption, an oxygen vacancy and a bare Pt were exposed (structure ii). Then, a gas-phase O2 adsorbed at the vacancy site and then dissociated into two *O with a large exothermicity and an activation energy of 0.15 eV (TS-2) (structures iii to iv). Afterward, a gas-phase CO adsorbed on

the bare Pt site with an adsorption energy of $-0.80~{\rm eV}$ (structure v). In the following step, the second CO oxidation between this newly adsorbed *CO and nearby *O released 1.44 eV energy (structures v to vi) and showed a small activation energy of 0.75 eV (TS-3). With another CO adsorbed on the structure vi ($E_{\rm ads}=-2.36~{\rm eV}$), the catalyst turned into the initial state. Overall, the first CO oxidation was confirmed as the rate-determining step (RDS) for the whole CO oxidation process on the Pt_{ASL}/CA catalyst with an activation energy of 1.78 eV.

On the Pt_{ASL}/CA-e catalyst, as shown in Figure 6 and Table S7, the CO oxidation mechanism was proposed starting from the defective embedded Pt_{ASL} (with two terrace O_v) fully covered by *CO (structure i). Initially, a gas-phase O₂ occupied the terrace O_v with an adsorption energy of -0.47 eV (structure ii). In this case, the interface O was activated by the adsorbed *O₂, with its O_v formation energy decreased from 2.25 to 0.48 eV. In contrast, the O_v formation energies for O in Pt-O-Pt and Pt-O-Ce on structure ii were calculated as 1.44 and 2.09 eV, respectively, indicating that the O species involved in the CO oxidation should come from the interface CeO₂. Accordingly, the activation energy of *CO reacting with this interface O (TS-1) was calculated as 0.62 eV. After releasing the first CO₂ (structure iii), an interface oxygen vacancy was formed and a bare Pt was exposed. Then, a gasphase CO covered the bare Pt with a large exothermicity of 1.57 eV (structure iv). Thereafter, the chemisorbed *O₂ was activated at O_v on the interface CeO₂ with an elongated O-O bond of 1.45 Å (structure iv) and then dissociated into one terrace *O and one interface *O (structure v). The activation energy and reaction energy of the O2 dissociation step were calculated as 0.71 and 0.25 eV, respectively. Once the interface *O was restored, the second CO oxidation between *CO and interface *O proceeded with an intrinsic energy barrier of 0.57 eV (TS-3). However, because the former *O₂ dissociation step was endothermic by 0.25 eV, the apparent activation energy of the second CO oxidation should be corrected to 0.82 eV. After CO₂ desorption (structure vi), it was energetically favorable for a gas-phase CO to adsorb on the exposed Pt atom (structure vii). Finally, the terrace *O migrated facilely to the interface site (~0 eV barrier) and regenerated the catalyst with an exothermicity of 0.44 eV. In agreement with the reaction kinetics results for CO and O2, such multistep CO oxidation followed the MvK mechanism. The RDS included the O2 dissociation and the second CO oxidation on Pt_{ASL}/CA-e, with an apparent activation energy of 0.82 eV (from structures iv to vi). Such activation energy for the RDS on Pt_{ASL}/CA-e was much lower than that on Pt_{ASL}/CA (1.78 eV), well explaining why the Pt_{ASL}/CA-e catalyst significantly outperformed the Pt_{ASI}/CA catalyst for low-temperature CO oxidation.

In short summary, based on experimental results and DFT calculations, the functions of embedded Pt_{ASL} and interface CeO₂ within the Pt_{ASL}/CeO₂-e catalyst were clearly revealed to better understand its superior CO oxidation activity. Owing to the appropriate CO chemisorption energy on the embedded Pt_{ASL} structure (-1.38 eV), the Pt-CO bonding was neither too weak nor too strong. According to Sabatier's principle in heterogeneous catalysis, the embedded Pt_{ASL} structure could effectively serve as the CO concentrator for *CO enrichment on Pt sites and at the same time prevent the CO poisoning effect that was widely present and detrimental for Pt SACs.²¹ With the presence of the embedded Pt_{ASL} structure, more interestingly, the oxygen vacancies could be easily created on

the interface CeO_2 , which provided highly efficient sites for O_2 adsorption, activation, and dissociation (Figure 6). Therefore, the interface CeO_2 activated by embedded Pt_{ASL} played multiple important roles in activating and donating *O for *CO consumption. The overall CO oxidation proceeded at the interface between embedded Pt_{ASL} and interface CeO_2 with a low activation energy of 0.82 eV, synergistically leading to the excellent performance of the Pt_{ASL}/CA -e catalyst for low-temperature CO oxidation.

CONCLUSIONS

Herein, we demonstrated an effective surface defect enrichment strategy to create rich defects on the CeO2-Al2O3 support as Pt anchoring sites. Based on comprehensive structural characterization results and DFT calculations, it was clearly found that Pt₁ catalysts with different local coordination environments could be obtained on CeO2-Al₂O₃ supports with and without defect enrichment. The difference in the local coordination environments of Pt, species not only impacted the CO adsorption behavior and CO oxidation activity, but also significantly influenced the structural evolution of Pt1 into more active Pt clusters including Pt_{ASL} (atomic single-layer clusters) and Pt_C (multilayer clusters) during the reduction activation process. In detail, the embedded Pt_{ASL} and Pt_C structures in the CeO₂ surface matrix could be fabricated from the embedded Pt₁ sites, while the adsorbed PtASL and PtC structures on the CeO2 surface could be generated from the adsorbed Pt1 sites. Among these Pt structures, the embedded Pt_{ASL} structure in the CeO_2 lattice matrix was confirmed as the most active site for converting CO to CO₂. Further analysis suggested that the embedded Pt_{ASL} structure favored the CO adsorption with appropriate CO binding strength and could efficiently activate the lattice oxygen at the Pt_{ASL}-CeO₂ interface simultaneously, thus leading to superior low-temperature CO oxidation activity.

ASSOCIATED CONTENT

Supporting Information

The Supporting Information is available free of charge at https://pubs.acs.org/doi/10.1021/jacs.2c08902.

Experimental and methods section, and other supporting results and discussion on reaction data, catalyst characterization, kinetics and mechanism study, and DFT calculations (PDF)

AUTHOR INFORMATION

Corresponding Authors

ı

Yue Lu — Beijing Key Laboratory of Microstructure and Properties of Solids, Faculty of Materials and Manufacturing, Beijing University of Technology, Beijing 100124, China; orcid.org/0000-0001-9800-3792; Email: luyue@bjut.edu.cn

Hongliang Xin — Department of Chemical Engineering, Virginia Polytechnic Institute and State University, Blacksburg, Virginia 24061, United States; orcid.org/0000-0001-9344-1697; Email: hxin@vt.edu

Fudong Liu — Department of Civil, Environmental, and Construction Engineering, Catalysis Cluster for Renewable Energy and Chemical Transformations (REACT), NanoScience Technology Center (NSTC), University of Central Florida, Orlando, Florida 32816, United States; orcid.org/0000-0001-8771-5938; Phone: 407-823-6219; Email: fudong.liu@ucf.edu

Authors

- Shaohua Xie Department of Civil, Environmental, and Construction Engineering, Catalysis Cluster for Renewable Energy and Chemical Transformations (REACT), NanoScience Technology Center (NSTC), University of Central Florida, Orlando, Florida 32816, United States; orcid.org/0000-0003-1550-7421
- Liping Liu Department of Chemical Engineering, Virginia Polytechnic Institute and State University, Blacksburg, Virginia 24061, United States; orcid.org/0000-0001-7543-1751
- Chunying Wang Center for Excellence in Regional Atmospheric Environment, Institute of Urban Environment, Chinese Academy of Sciences, Xiamen 361021, China
- Sufeng Cao Department of Chemical and Biological Engineering, Tufts University, Medford, Massachusetts 02155, United States
- Weijian Diao Department of Chemical and Biological Engineering, Villanova University, Villanova, Pennsylvania 19085, United States
- Jiguang Deng College of Environmental and Energy Engineering, Beijing University of Technology, Beijing 100124, China; orcid.org/0000-0001-7768-3688
- Wei Tan Department of Civil, Environmental, and Construction Engineering, Catalysis Cluster for Renewable Energy and Chemical Transformations (REACT), NanoScience Technology Center (NSTC), University of Central Florida, Orlando, Florida 32816, United States; State Key Laboratory of Pollution Control and Resource Reuse, School of Environment; Jiangsu Key Laboratory of Vehicle Emissions Control, Nanjing University, Nanjing 210023, China; orcid.org/0000-0002-1481-9346
- Lu Ma National Synchrotron Light Source II (NSLS-II), Brookhaven National Laboratory, Upton, New York 11973, United States
- Steven N. Ehrlich National Synchrotron Light Source II (NSLS-II), Brookhaven National Laboratory, Upton, New York 11973, United States
- Yaobin Li Center for Excellence in Regional Atmospheric Environment, Institute of Urban Environment, Chinese Academy of Sciences, Xiamen 361021, China
- Yan Zhang Center for Excellence in Regional Atmospheric Environment, Institute of Urban Environment, Chinese Academy of Sciences, Xiamen 361021, China; orcid.org/ 0000-0002-5423-8255
- Kailong Ye Department of Civil, Environmental, and Construction Engineering, Catalysis Cluster for Renewable Energy and Chemical Transformations (REACT), NanoScience Technology Center (NSTC), University of Central Florida, Orlando, Florida 32816, United States
- Maria Flytzani-Stephanopoulos Department of Chemical and Biological Engineering, Tufts University, Medford, Massachusetts 02155, United States

Complete contact information is available at: https://pubs.acs.org/10.1021/jacs.2c08902

Author Contributions

[¶]S.X. and L.L. contributed equally.

Funding

This work was supported by the Startup Fund (F.L.) from the University of Central Florida (UCF). S.X. received the support from the Preeminent Postdoctoral Program (P3) at UCF. L.L. received the Hord Scholarship from the Department of Chemical Engineering at Virginia Polytechnic Institute and State University. H.X. received the NSF CAREER program (CBET-1845531). Y.L. received support from the Beijing Innovation Team Building Program (IDHT20190503), the National Natural Science Foundation of China (12074016, 12274009), and Technology Development Project of Beijing Municipal Education Commission (KM202110005003).

Notes

The authors declare no competing financial interest. &M.F.-S. passed away on October 28, 2019.

ACKNOWLEDGMENTS

F.L. sincerely thanks Dr. Marcos Schöneborn at Sasol for providing raw materials in catalyst synthesis. This research used the beamline 7-BM (QAS) of the National Synchrotron Light Source II, a U.S. Department of Energy (DOE) Office of Science User Facility operated for the DOE Office of Science by the Brookhaven National Laboratory under contract no. DE-SC0012704. H.X. acknowledges the computational resource provided by the advanced research computing at Virginia Polytechnic Institute and State University.

REFERENCES

- (1) Gawande, M. B.; Ariga, K.; Yamauchi, Y. Single-Atom Catalysts. *Small* **2021**, *17*, No. e2101584.
- (2) Bruix, A.; Lykhach, Y.; Matolinova, I.; Neitzel, A.; Skala, T.; Tsud, N.; Vorokhta, M.; Stetsovych, V.; Sevcikova, K.; Myslivecek, J.; Fiala, R.; Vaclavu, M.; Prince, K. C.; Bruyere, S.; Potin, V.; Illas, F.; Matolin, V.; Libuda, J.; Neyman, K. M. Maximum Noble-Metal Efficiency in Catalytic Materials: Atomically Dispersed Surface Platinum. Angew. Chem., Int. Ed. 2014, 53, 10525–10530.
- (3) Lang, R.; Xi, W.; Liu, J. C.; Cui, Y. T.; Li, T.; Lee, A. F.; Chen, F.; Chen, Y.; Li, L.; Li, L.; Lin, J.; Miao, S.; Liu, X.; Wang, A. Q.; Wang, X.; Luo, J.; Qiao, B.; Li, J.; Zhang, T. Non Defect-Stabilized Thermally Stable Single-Atom Catalyst. *Nat. Commun.* **2019**, *10*, 234.
- (4) Li, X.; Huang, Y.; Liu, B. Catalyst: Single-Atom Catalysis: Directing the Way toward the Nature of Catalysis. *Chem* **2019**, *5*, 2733–2735.
- (5) Li, Z.; Wang, D.; Wu, Y.; Li, Y. Recent Advances in the Precise Control of Isolated Single-Site Catalysts by Chemical Methods. *Natl. Sci. Rev.* **2018**, *5*, 673–689.
- (6) Liu, Q.; Zhang, Z. Platinum Single-Atom Catalysts: a Comparative Review towards Effective Characterization. *Catal. Sci. Technol.* **2019**, *9*, 4821–4834.
- (7) Malta, G.; Kondrat, S. A.; Freakley, S. J.; Davies, C. J.; Lu, L.; Dawson, S.; Thetford, A.; Gibson, E. K.; Morgan, D. J.; Jones, W.; Wells, P. P.; Johnston, P.; Catlow, C. R. A.; Kiely, C. J.; Hutchings, G. J. Identification of Single-Site Gold Catalysis in Acetylene Hydrochlorination. *Science* **2017**, *355*, 1399–1403.
- (8) Zhang, Z.; Zhu, Y.; Asakura, H.; Zhang, B.; Zhang, J.; Zhou, M.; Han, Y.; Tanaka, T.; Wang, A.; Zhang, T.; Yan, N. Thermally Stable Single Atom Pt/m-Al₂O₃ for Selective Hydrogenation and CO Oxidation. *Nat. Commun.* **2017**, *8*, 16100.
- (9) Wang, L.; Chen, M. X.; Yan, Q. Q.; Xu, S. L.; Chu, S. Q.; Chen, P.; Lin, Y.; Liang, H.-W. A Sulfur-Tethering Synthesis Strategy toward High-Loading Atomically Dispersed Noble Metal Catalysts. *Sci. Adv.* **2019**, *5*, No. eaax6322.
- (10) Christopher, P. Single-Atom Catalysts: Are All Sites Created Equal? ACS Energy Lett. 2019, 4, 2249-2250.
- (11) DeRita, L.; Resasco, J.; Dai, S.; Boubnov, A.; Thang, H. V.; Hoffman, A. S.; Ro, I.; Graham, G. W.; Bare, S. R.; Pacchioni, G.; Pan,

- X.; Christopher, P. Structural Evolution of Atomically Dispersed Pt Catalysts Dictates Reactivity. *Nat. Mater.* **2019**, *18*, 746–751.
- (12) Nie, L.; Mei, D. H.; Xiong, H. F.; Peng, B.; Ren, Z. B.; Hernandez, X. I. P.; DeLaRiva, A.; Wang, M.; Engelhard, M. H.; Kovarik, L.; Datye, A. K.; Wang, Y. Activation of Surface Lattice Oxygen in Single-Atom Pt/CeO₂ for Low-Temperature CO Oxidation. *Science* **2017**, 358, 1419–1423.
- (13) Li, S.; Liu, J.; Yin, Z.; Ren, P.; Lin, L.; Gong, Y.; Yang, C.; Zheng, X.; Cao, R.; Yao, S.; Deng, Y.; Liu, X.; Gu, L.; Zhou, W.; Zhu, J.; Wen, X.; Xu, B.; Ma, D. Impact of the Coordination Environment on Atomically Dispersed Pt Catalysts for Oxygen Reduction Reaction. *ACS Catal.* **2019**, *10*, 907–913.
- (14) Li, X.; Rong, H.; Zhang, J.; Wang, D.; Li, Y. Modulating the Local Coordination Environment of Single-Atom Catalysts for Enhanced Catalytic Performance. *Nano Res.* **2020**, *13*, 1842–1855.
- (15) Liu, D.; He, Q.; Ding, S.; Song, L. Structural Regulation and Support Coupling Effect of Single-Atom Catalysts for Heterogeneous Catalysis. *Adv. Energy Mater.* **2020**, *10*, No. 2001482.
- (16) Ren, Y.; Tang, Y.; Zhang, L.; Liu, X.; Li, L.; Miao, S.; Sheng Su, D.; Wang, A.; Li, J.; Zhang, T. Unraveling the Coordination Structure-Performance Relationship in Pt₁/Fe₂O₃ Single-Atom Catalyst. *Nat. Commun.* **2019**, *10*, 4500.
- (17) Resasco, J.; Christopher, P. Atomically Dispersed Pt-group Catalysts: Reactivity, Uniformity, Structural Evolution, and Paths to Increased Functionality. *J. Phys. Chem. Lett.* **2020**, *11*, 10114–10123.
- (18) Jeong, H.; Shin, D.; Kim, B. S.; Bae, J.; Shin, S.; Choe, C.; Han, J. W.; Lee, H. Controlling the Oxidation State of Pt Single Atoms for Maximizing Catalytic Activity. *Angew. Chem., Int. Ed.* **2020**, *59*, 20691–20696.
- (19) Jiang, D.; Yao, Y.; Li, T.; Wan, G.; Pereira-Hernandez, X. I.; Lu, Y.; Tian, J.; Khivantsev, K.; Engelhard, M. H.; Sun, C.; Garcia-Vargas, C. E.; Hoffman, A. S.; Bare, S. R.; Datye, A. K.; Hu, L.; Wang, Y. Tailoring the Local Environment of Platinum in Single-Atom Pt₁/CeO₂ Catalysts for Robust Low-Temperature CO Oxidation. *Angew. Chem., Int. Ed.* **2021**, *60*, 26054–26062.
- (20) Meier, M.; Hulva, J.; Jakub, Z.; Kraushofer, F.; Bobić, M.; Bliem, R.; Setvin, M.; Schmid, M.; Diebold, U.; Franchini, C.; Parkinson, G. S. CO Oxidation by Pt₂/Fe₃O₄: Metastable Dimer and Support Configurations Facilitate Lattice Oxygen Extraction. *Sci. Adv.* **2022**, *8*, No. eabn4580.
- (21) Ding, K. L.; Gulec, A.; Johnson, A. M.; Schweitzer, N. M.; Stucky, G. D.; Marks, L. D.; Stair, P. C. Identification of Active Sites in CO Oxidation and Water-Gas Shift over Supported Pt Catalysts. *Science* **2015**, *350*, 189–192.
- (22) Wang, H.; Liu, J. X.; Allard, L. F.; Lee, S.; Liu, J.; Li, H.; Wang, J.; Wang, J.; Oh, S. H.; Li, W.; Flytzani-Stephanopoulos, M.; Shen, M.; Goldsmith, B. R.; Yang, M. Surpassing the Single-Atom Catalytic Activity Limit through Paired Pt-O-Pt Ensemble Built from Isolated Pt₁ Atoms. *Nat. Commun.* **2019**, *10*, 3808.
- (23) Zhang, J.; Yang, H.; Liu, B. Coordination Engineering of Single-Atom Catalysts for the Oxygen Reduction Reaction: A Review. *Adv. Energy Mater.* **2021**, *11*, No. 2002473.
- (24) Chen, M. S.; Goodman, D. W. The Structure of Catalytically Active Gold on Titania. *Science* **2004**, *306*, 252–255.
- (25) Lopez, N. The Adhesion and Shape of Nanosized Au Particles in a Au/TiO₂ Catalyst. *J. Catal.* **2004**, 225, 86–94.
- (26) He, Y.; Liu, J. C.; Luo, L.; Wang, Y. G.; Zhu, J.; Du, Y.; Li, J.; Mao, S. X.; Wang, C. Size-Dependent Dynamic Structures of Supported Gold Nanoparticles in CO Oxidation Reaction Condition. *Proc. Natl. Acad. Sci. U. S. A.* **2018**, *115*, 7700–7705.
- (27) Kwak, J. H.; Hu, J. Z.; Mei, D. H.; Yi, C. W.; Kim, D. H.; Peden, C. H. F.; Allard, L. F.; Szanyi, J. Coordinatively Unsaturated Al^{3+} Centers as Binding Sites for Active Catalyst Phases of Platinum on γ -Al₂O₃. Science **2009**, 325, 1670–1673.
- (28) Mei, D.; Kwak, J. H.; Hu, J.; Cho, S. J.; Szanyi, J.; Allard, L. F.; Peden, C. H. F. Unique Role of Anchoring Penta-Coordinated Al³⁺ Sites in the Sintering of γ -Al₂O₃-Supported Pt Catalysts. *J. Phys. Chem. Lett.* **2010**, *1*, 2688–2691.

- (29) Lee, J.; Jang, E. J.; Oh, D. G.; Szanyi, J.; Kwak, J. H. Morphology and size of Pt on Al₂O₃: The Role of Specific Metal-Support Interactions between Pt and Al₂O₃. *J. Catal.* **2020**, 385, 204–212.
- (30) Shi, L.; Deng, G. M.; Li, W. C.; Miao, S.; Wang, Q. N.; Zhang, W. P.; Lu, A. H. Al₂O₃ Nanosheets Rich in Pentacoordinate Al(3+) Ions Stabilize Pt-Sn Clusters for Propane Dehydrogenation. *Angew. Chem., Int. Ed.* **2015**, *54*, 13994–13998.
- (31) Zhu, Y.; An, Z.; Song, H.; Xiang, X.; Yan, W.; He, J. Lattice-Confined Sn (IV/II) Stabilizing Raft-Like Pt Clusters: High Selectivity and Durability in Propane Dehydrogenation. *ACS Catal.* **2017**, *7*, 6973–6978.
- (32) Xiong, H.; Kunwar, D.; Jiang, D.; García-Vargas, C. E.; Li, H.; Du, C.; Canning, G.; Pereira-Hernandez, X. I.; Wan, Q.; Lin, S.; Purdy, S. C.; Miller, J. T.; Leung, K.; Chou, S. S.; Brongersma, H. H.; ter Veen, R.; Huang, J.; Guo, H.; Wang, Y.; Datye, A. K. Engineering Catalyst Supports to Stabilize PdO_x Two-Dimensional Rafts for Water-Tolerant Methane Oxidation. *Nat. Catal.* **2021**, *4*, 830–839.
- (33) Ferré, G.; Aouine, M.; Bosselet, F.; Burel, L.; Cadete Santos Aires, F. J.; Geantet, C.; Ntais, S.; Maurer, F.; Casapu, M.; Grunwaldt, J. D.; Epicier, T.; Loridant, S.; Vernoux, P. Exploiting the Dynamic Properties of Pt on Ceria for Low-Temperature Co Oxidation. *Catal. Sci. Technol.* **2020**, *10*, 3904–3917.
- (34) Ke, J.; Zhu, W.; Jiang, Y.; Si, R.; Wang, Y. J.; Li, S. C.; Jin, C.; Liu, H.; Song, W. G.; Yan, C. H.; Zhang, Y. W. Strong Local Coordination Structure Effects on Subnanometer PtO_x Clusters over CeO₂ Nanowires Probed by Low-Temperature CO Oxidation. *ACS Catal.* **2015**, *5*, 5164–5173.
- (35) Zhan, W.; He, Q.; Liu, X.; Guo, Y.; Wang, Y.; Wang, L.; Guo, Y.; Borisevich, A. Y.; Zhang, J.; Lu, G.; Dai, S. A Sacrificial Coating Strategy Toward Enhancement of Metal-Support Interaction for Ultrastable Au Nanocatalysts. *J. Am. Chem. Soc.* **2016**, *138*, 16130–16139.
- (36) Tang, H. L.; Su, Y.; Zhang, B. S.; Lee, A. F.; Isaacs, M. A.; Wilson, K.; Li, L.; Ren, Y. G.; Huang, J. H.; Haruta, M.; Qiao, B. T.; Liu, X.; Jin, C. Z.; Su, D. S.; Wang, J. H.; Zhang, T. Classical Strong Metal-Support Interactions between Gold Nanoparticles and Titanium Dioxide. *Sci. Adv.* 2017, 3, No. e1700231.
- (37) Daniel, M.; Loridant, S. Probing Reoxidation Sites by *in situ* Raman Spectroscopy: Differences between Reduced CeO₂ and Pt/CeO₂. *J. Raman Spectrosc.* **2012**, *43*, 1312–1319.
- (38) Schilling, C.; Hofmann, A.; Hess, C.; Ganduglia-Pirovano, M. V. Raman Spectra of Polycrystalline CeO₂: A Density Functional Theory Study. *J. Phys. Chem. C* **2017**, *121*, 20834–20849.
- (39) Artiglia, L.; Orlando, F.; Roy, K.; Kopelent, R.; Safonova, O.; Nachtegaal, M.; Huthwelker, T.; van Bokhoven, J. A. Introducing Time Resolution to Detect Ce(3+) Catalytically Active Sites at the Pt/CeO₂ Interface through Ambient Pressure X-ray Photoelectron Spectroscopy. *J. Phys. Chem. Lett.* **2017**, *8*, 102–108.
- (40) Daelman, N.; Capdevila-Cortada, M.; Lopez, N. Dynamic Charge and Oxidation State of Pt/CeO₂ Single-Atom Catalysts. *Nat. Mater.* **2019**, *18*, 1215–1221.
- (41) Tang, Y.; Wang, Y. G.; Li, J. Theoretical Investigations of Pt₁@ CeO₂ Single-Atom Catalyst for CO Oxidation. *J. Phys. Chem. C* **2017**, 121, 11281–11289.
- (42) Zhang, W.; Pu, M.; Lei, M. Theoretical Studies on the Stability and Reactivity of the Metal-Doped $CeO_2(100)$ Surface: Toward H_2 Dissociation and Oxygen Vacancy Formation. *Langmuir* **2020**, *36*, 5891–5901.
- (43) Wang, Y.; Liu, Z.; Confer, M. P.; Li, J.; Wang, R. In-Situ DRIFTS Study of Chemically Etched CeO₂ Nanorods Supported Transition Metal Oxide Catalysts. *Mol. Catal.* **2021**, *509*, No. 111629.
- (44) Maurer, F.; Jelic, J.; Wang, J.; Gänzler, A.; Dolcet, P.; Wöll, C.; Wang, Y.; Studt, F.; Casapu, M.; Grunwaldt, J.-D. Tracking the Formation, Fate and Consequence for Catalytic Activity of Pt Single Sites on CeO₂. *Nat. Catal.* **2020**, *3*, 824–833.
- (45) Gänzler, A. M.; Casapu, M.; Maurer, F.; Störmer, H.; Gerthsen, D.; Ferré, G.; Vernoux, P.; Bornmann, B.; Frahm, R.; Murzin, V.; Nachtegaal, M.; Votsmeier, M.; Grunwaldt, J.-D. Tuning the Pt/CeO_2

Interface by in situ Variation of the Pt Particle Size. ACS Catal. 2018, 8, 4800-4811.

- (46) Xie, S.; Tan, W.; Wang, C.; Arandiyan, H.; Garbrecht, M.; Ma, L.; Ehrlich, S. N.; Xu, P.; Li, Y.; Zhang, Y.; Collier, S.; Deng, J.; Liu, F. Structure-Activity Relationship of Pt Catalyst on Engineered Ceria-Alumina Support for CO Oxidation. J. Catal. 2022, 405, 236-248.
- (47) Sabatier, P. La Catalyse en Chimie Organique, par Paul Sabatier; Béranger, C., Ed., 1913; p 256.
- (48) Lu, Y.; Zhou, S.; Kuo, C. T.; Kunwar, D.; Thompson, C.; Hoffman, A. S.; Boubnov, A.; Lin, S.; Datye, A. K.; Guo, H.; Karim, A. M. Unraveling the Intermediate Reaction Complexes and Critical Role of Support-Derived Oxygen Atoms in CO Oxidation on Single-Atom Pt/CeO₂. ACS Catal. **2021**, 11, 8701–8715.
- (49) Wang, C.; Gu, X. K.; Yan, H.; Lin, Y.; Li, J.; Liu, D.; Li, W. X.; Lu, J. Water-Mediated Mars-Van Krevelen Mechanism for CO Oxidation on Ceria-Supported Single-Atom Pt, Catalyst. ACS Catal. **2016**, 7, 887-891.
- (50) Yoo, M.; Yu, Y.-S.; Ha, H.; Lee, S.; Choi, J.-S.; Oh, S.; Kang, E.; Choi, H.; An, H.; Lee, K.-S.; Park, J. Y.; Celestre, R.; Marcus, M. A.; Nowrouzi, K.; Taube, D.; Shapiro, D. A.; Jung, W.; Kim, C.; Kim, H. Y. A Tailored Oxide Interface Creates Dense Pt Single-Atom Catalysts with High Catalytic Activity. Energy Environ. Sci. 2020, 13, 1231-1239.
- (51) Wang, T.; Xing, J. Y.; Jia, A. P.; Tang, C.; Wang, Y. J.; Luo, M. F.; Lu, J. Q. CO Oxidation over Pt/Cr_{1.3}Fe_{0.7}O₃ Catalysts: Enhanced Activity on Single Pt Atom by H2O Promotion. J. Catal. 2020, 382, 192-203.
- (52) Ha, H.; Yoon, S.; An, K.; Kim, H. Y. Catalytic CO Oxidation over Au Nanoparticles Supported on CeO2 Nanocrystals: Effect of the Au-CeO₂ Interface. ACS Catal. 2018, 8, 11491-11501.
- (53) Han, M. M.; Wang, X. J.; Shen, Y. N.; Tang, C. H.; Li, G. S.; Smith, R. L. Preparation of Highly Active, Low Au-Loaded, Au/CeO₂ Nanoparticle Catalysts That Promote CO Oxidation at Ambient Temperatures. J. Phys. Chem. C 2010, 114, 793-798.
- (54) Chen, S.; Luo, L.; Jiang, Z.; Huang, W. Size-Dependent Reaction Pathways of Low-Temperature CO Oxidation on Au/CeO₂ Catalysts. ACS Catal. 2015, 5, 1653-1662.
- (55) Vincent, J. L.; Crozier, P. A. Atomic Level Fluxional Behavior and Activity of CeO2-Supported Pt Catalysts for CO Oxidation. Nat. Commun. 2021, 12, 5789.
- (56) Bosio, N.; Di, M.; Skoglundh, M.; Carlsson, P. A.; Grönbeck, H. Interface Reactions Dominate Low-Temperature CO Oxidation Activity over Pt/CeO₂. J. Phys. Chem. C 2022, 126, 16164-16171.

□ Recommended by ACS

Low-Temperature Catalytic NO Reduction with CO by **Subnanometric Pt Clusters**

Estefanía Fernández, Avelino Corma, et al.

NOVEMBER 15 2019

ACS CATALYSIS

READ 2

Cluster Catalysis with Lattice Oxygen: Tracing Oxygen Transport from a Magnetite (001) Support onto Small Pt Clusters

Sebastian Kaiser, Friedrich Esch, et al.

JULY 16, 2021

ACS CATALYSIS

READ **C**

Interface Reactions Dominate Low-Temperature CO Oxidation Activity over Pt/CeO,

Noemi Bosio, Henrik Grönbeck, et al.

SEPTEMBER 14, 2022

THE JOURNAL OF PHYSICAL CHEMISTRY C

RFAD 17

Water-Assisted Growth of Cobalt Oxide and Cobalt Hydroxide Overlayers on the Pt₃Co(111) Surface

Jeongjin Kim, Jeong Young Park, et al.

NOVEMBER 21, 2019

ACS APPLIED ENERGY MATERIALS

READ **C**

Get More Suggestions >